J. Fluid Mech. (2002), *vol.* 454, *pp.* 365–386. © 2002 Cambridge University Press
DOI: 10.1017/S0022112001007170 Printed in the United Kingdom

On converging shock waves of spherical and polyhedral form

By DONALD W. SCHWENDEMAN

Department of Mathematical Sciences, Rensselaer Polytechnic Institute, Troy, NY 12180, USA

(Received 10 April 2001 and in revised form 31 July 2001)

The behaviour of converging spherical shock waves is considered using Whitham's theory of geometrical shock dynamics. An analysis of converging shocks whose initial shape takes the form of regular polyhedra is presented. The analysis of this problem is motivated by the earlier work on converging cylindrical shocks discussed in Schwendeman & Whitham (1987). In that paper, exact solutions were reported for converging polygonal shocks in which the initial shape re-forms repeatedly as the shock contracts. For the polyhedral case, the analysis is performed both analytically and numerically for an equivalent problem involving shock propagation in a converging channel with triangular cross-section. It is found that a repeating sequence of shock surfaces composed of nearly planar pieces develops, although the initial planar surface does not re-form, and that the increase in strength of the shock at each iterate in the sequence follows the same behaviour as for a converging spherical shock independent of the convergence angle of the channel. In this sense, the shocks are stable and the result is analogous to that found in the two-dimensional case. A numerical study of converging spherical shocks subject to smooth initial perturbations in strength shows a strong tendency to form surfaces composed of nearly planar pieces suggesting that the stability result is fairly general.

1. Introduction

In the original description of the theory of geometrical shock dynamics (Whitham 1957), it was shown that a converging cylindrical shock wave would be unstable to small disturbances. As these disturbances grow, discontinuities in Mach number and slope along the leading shock front, referred to as 'shock-shocks' in the theory, would develop. The subsequent behaviour of the converging shock and hence the ultimate question of stability was not analysed in Whitham (1957). In a later paper (Schwendeman & Whitham 1987), it was found that the behaviour of converging cylindrical shock waves that take the form of regular polygons could be analysed exactly within the theory. Each vertex of the polygon opens up to form a Mach stem which then proceeds to grow and consume the incident shocks from the neighbouring sides. If the initial strength of the shock is uniform, then the Mach stems formed at the vertices grow and eventually meet at the same time thus re-forming the polygon with a contraction in scale and an increase in strength. The process repeats, and it was shown that the increase in Mach number at each step behaves according to the same law as for a converging cylindrical shock independent of the number of sides of the original polygon. It was concluded that converging cylindrical shocks are stable to perturbations that take the form of regular polygons.

Numerical calculations of the behaviour of converging cylindrical shocks subject

https://doi.org/10.1017/S0022112001007170 Published online by Cambridge University Press

to smooth perturbations were also presented in Schwendeman & Whitham (1987), and these results showed that converging shocks have a strong tendency to form planar sides and polygonal shock shapes. A similar behaviour has been observed experimentally by Takayama, Kleine & Grönig (1987) and by Watanabe & Takayama (1991). In the latter paper, simulations of the full equations of gasdynamics were conducted and shown to agree with the experimental observations. Thus, the stability result for regular polygons appears to be fairly general.

Brief comments were made in Schwendeman & Whitham (1987) concerning the behaviour of converging spherical shocks. For initial shock shapes that take the form of regular polyhedra, each vertex and edge would form a Mach face similar to that for the cylindrical case. However, an exact solution for the spherical case was not found nor was a detailed analysis given. It was conjectured that the original polyhedral shape would not repeat but, rather, more and more Mach faces would develop leading to a closer approximation of a sphere and stability. In Schwendeman (1993), a numerical scheme for shock propagation in two and three dimensions was presented. In this work, the behaviour of converging shocks in three dimensions, among other problems, was considered. It was found that smooth, three-dimensional perturbations of converging cylindrical and spherical shocks tended to form nearly planar Mach stems similar to that observed in the two-dimensional case. The behaviour of an average fractional change in radius, $\Delta R/R$, for the converging shocks was calculated for each case and found to decay, thus suggesting stabilty. The spherical shock case was considered under the constraint of conical guide walls in order to avoid the geometric singularities at the two poles imposed by a mapping to a Cartesian grid used in the numerical scheme. The numerical method to be presented here uses an unstructured grid based on triangular prism cells in part to avoid this difficulty.

Additional studies of converging shocks using geometrical shock dynamics have been discussed in Gardner, Book & Bernstein (1982) following the work in Fong & Ahlborn (1979). Both of these studies concentrated on the behaviour of converging cylindrical and spherical shocks subject to initial perturbations (possibly large) that took the shape of an isolated bulge. For the spherical case, axial symmetry was assumed. The result was essentially the same as that discussed above. The initial bulge flattened and ultimately formed shock-shocks and planar Mach stem-like shocks in agreement with the observations discussed above. In Apazidis & Lesser (1996), converging shocks were generated by reflection from the wall of a cylindrical confinement, and polygonal shock shapes appeared in cases where the confinement boundary possessed smooth perturbations about a circular shape.

In this paper, we study the behaviour and stability of converging spherical shocks. The analysis is carried out using the approximate theory of geometrical shock dynamics, but this theory is believed to be particularly accurate for converging shocks in part because of the excellent agreement with Guderley's similarity solution (Guderley 1942) for cylindrical and spherical shocks (see Whitham 1974). We begin by re-examining the case of converging spherical shocks whose initial shape takes the form of regular polyhedra. An analysis of the propagation of these initial shock shapes is performed and the results are presented in § 2. It is found that, while it is possible for the initial shock to form another regular polyhedral shape at a later stage, it is not possible for the original polyhedral shape to re-form in a manner similar to the exact solution worked out for the two-dimensional case. This result, in agreement with the conjecture in Schwendeman & Whitham (1987), does not preclude the possibility that an initial shock in the shape of a regular polyhedron may propagate and evolve into other repeating configurations as it converges. In

https://doi.org/10.1017/S0022112001007170 Published online by Cambridge University Press

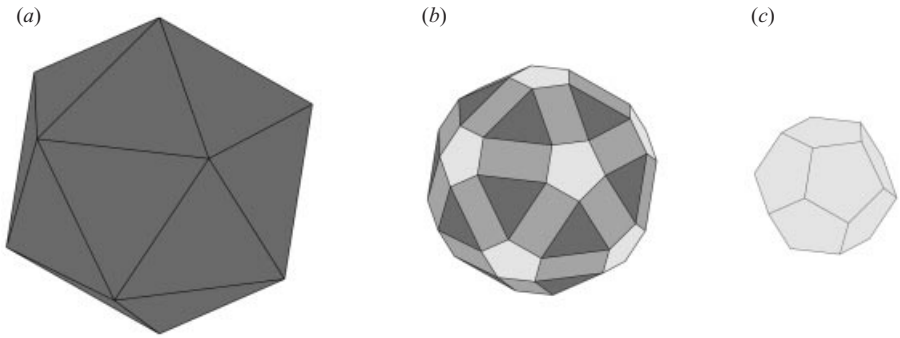


FIGURE 1. Converging polyhedral shock with 20 faces initially.

order to examine this possibility, a numerical method of calculation is developed in § 3, following the work in Schwendeman (1999), and is used in § 4 to calculate the three-dimensional propagation of a shock in a converging channel with a triangular cross-section. This geometry is motivated by the symmetries present in the regular polyhedra with 4, 8 and 20 faces. It is found that an initially planar shock evolves into a complicated but repeating sequence of shock surfaces composed of nearly planar pieces connected by shock-shocks. It is shown that the increase in the shock Mach number for each iterate in the sequence follows the same behaviour as a converging spherical shock, independent of the convergence angle of the channel. The result is thus analogous to the stability result in Schwendeman & Whitham (1987) for the two-dimensional case. Further numerical results are presented in § 5 for converging spherical shocks subject to smooth perturbations in their initial strength. It is found that the converging shocks tend to form shapes composed of (nearly) planar pieces indicating again that the stability result is fairly general.

2. Converging polyhedral shock shapes

Regular polyhedra are limited to ones with 4, 6, 8, 12 and 20 faces. For example, consider a converging shock whose initial shape takes the form of a regular polyhedron with 20 faces (an icosahedron) as shown in figure 1(*a*). As the shock collapses, each vertex and edge suffers a Mach reflection to form Mach faces as shown in figure 1(*b*). (There would also be reflected shocks from each shock-shock edge, but these are not determined explicitly in geometrical shock dynamics.) The shock formed at each vertex has the largest shock strength, and ultimately consumes the incident shocks from the initial polyhedral faces as well as the shocks formed by the Mach reflection from each original edge. If the incident shock pieces and the shocks from the edges vanish at the same time, then a regular polyhedra with 12 faces (a dodecahedron) is formed as shown in figure 1(*c*). The new polyhedral shock, as indicated in the figure, would be smaller than the original and would have an increased shock strength given by the converging shocks originating at each vertex. The condition that the incident shocks and the shocks from the edges vanish at the same time depends on the relative rates of advance of the shock-shocks from the original edges and vertices, and this condition is satisfied only in special cases as will be discussed below. For cases when this initial scenario occurs, the question becomes whether the shock returns in shape to the original icosahedron with a reduction in scale. A similar process may be

https://doi.org/10.1017/S0022112001007170 Published online by Cambridge University Press

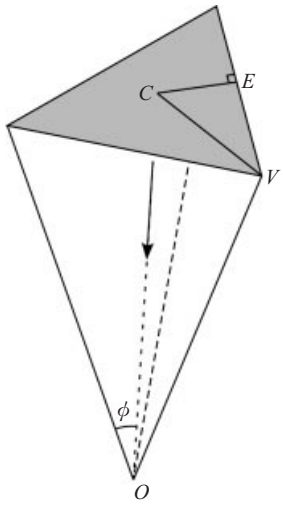


FIGURE 2. Converging channel geometry.

considered for the regular polyhedral pairs with 8 and 6 faces and with 4 and 4 faces. For the latter pair, the intermediate step would also be a tetrahedron.

For each of the three pairs we can identify planes of symmetry, and these may be viewed as effective walls within the theory. For the polyhedra with 4, 8 and 20 faces, planes of symmetry from each edge to the centre form converging channels with a triangular cross-section as shown in figure 2. Points C, E and V identify the face centre, an edge centre, and a vertex of the triangular face of the channel, respectively, and the point O lies at the point of convergence. The angle ϕ is the angle between the centreline OC and the line OV, and takes the (approximate) values 70.53°, 54.74° and 37.38° for polyhedra with 4, 8 and 20 faces, respectively. The problem of the behaviour of a converging shock whose initial shape takes the form of a regular polyhedron with 4, 8 or 20 faces may now be analysed by considering the propagation of an initially planar shock in the converging channel shown in the figure.

In order to analyse the evolution of the shock in the converging channel, it is convenient to consider the behaviour in the cut planes OCE and OEV as shown in figure 3. The planes are orthogonal to each other, but share the line OE so that they may be unfolded and laid flat as is done in the figure. The angles θ and ψ determine the behaviour of the shock propagation in each cut plane and these angles are related to the convergence angle ϕ by the formula

$$\tan\phi = 2\tan\theta = \frac{2\tan\psi}{\sqrt{3-\tan^2\psi}}. \tag{2.1}$$

The initial planar shock is seen in the figure connecting points C and E and has a Mach number equal to M_1, say. It experiences a Mach reflection by the effective wall OE and forms a shock-shock and a Mach stem with an increased Mach number M_2. The path of the shock-shocks from E (shown by the dotted line in the figure) makes an angle χ relative to the line OE. The angles θ and χ and the Mach numbers M_1 and M_2 are related by the shock-shock conditions

$$\tan\theta = \frac{(M_2^2-M_1^2)^{1/2}(A_1^2-A_2^2)^{1/2}}{A_2M_2+A_1M_1}, \quad \tan\chi = \frac{A_2}{A_1}\left\{\frac{1-(M_1/M_2)^2}{1-(A_2/A_1)^2}\right\}^{1/2} \tag{2.2}$$

https://doi.org/10.1017/S0022112001007170 Published online by Cambridge University Press

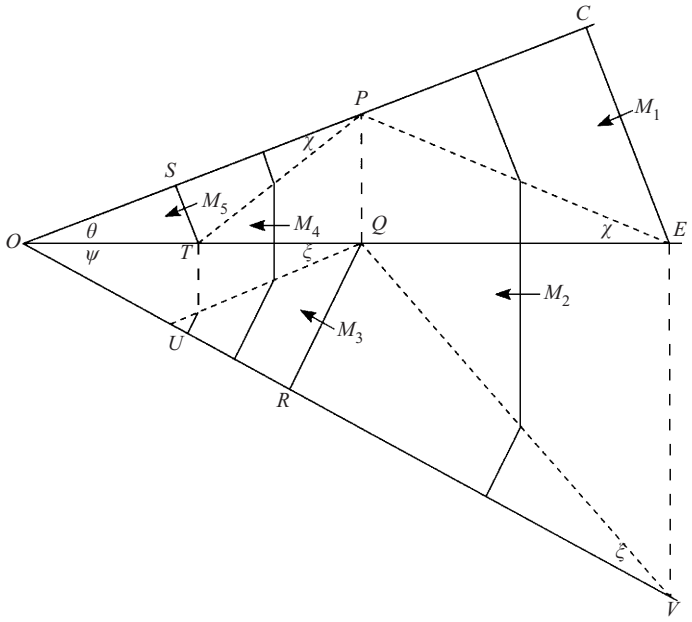


FIGURE 3. Behaviour of a converging shock in the cut planes OCE and OEV.

(see Whitham 1974). The ray-tube areas A_1 and A_2 are related to M_1 and M_2, respectively, by an assumed area–Mach number relation. For the case of a converging shock, the shock would become strong so that an appropriate form is

$$A = M^{-n}, \tag{2.3}$$

where the constant n is related to the ratio of specific heats γ for an ideal gas (e.g. $n = 5.0743$ when $\gamma = 1.4$) according to the area–Mach number relation initially proposed by Chisnell (1957) following the work of Chester (1954). Using (2.3), (2.2) reduces to

$$\tan\theta = \frac{(1-\sigma^2)^{1/2}(\sigma^{-2n}-1)^{1/2}}{1+\sigma^{1-n}}, \quad \tan\chi = \left(\frac{1-\sigma^2}{\sigma^{-2n}-1}\right)^{1/2}, \tag{2.4}$$

so that χ and $\sigma = M_1/M_2$ are determined by θ and n. The Mach stem formed by the Mach reflection at E, in turn, produces a Mach reflection at V and a Mach stem with shock Mach number M_3. (The dashed line connecting points E and V in the figure indicates the edge along the initial planar shock at the wall.) The angle ξ and ratio $\mu = M_2/M_3$ for this Mach reflection are determined by the angle ψ and n using the formulas

$$\tan\psi = \frac{(1-\mu^2)^{1/2}(\mu^{-2n}-1)^{1/2}}{1+\mu^{1-n}}, \quad \tan\xi = \left(\frac{1-\mu^2}{\mu^{-2n}-1}\right)^{1/2}, \tag{2.5}$$

similar to (2.4).

Top views of the corresponding shock surfaces are illustrated in figure 4. The initial planar shock shown in figure 4(a) experiences Mach reflections as described above to become the configuration shown in figure 4(b) composed of the incident shock in the centre surrounded by Mach stems from the reflections at the sides and corners of the converging channel. (The shock surfaces decrease in size but this is not shown in the figure.) If the shock-shock paths from E and V meet at the same time, then

https://doi.org/10.1017/S0022112001007170 Published online by Cambridge University Press

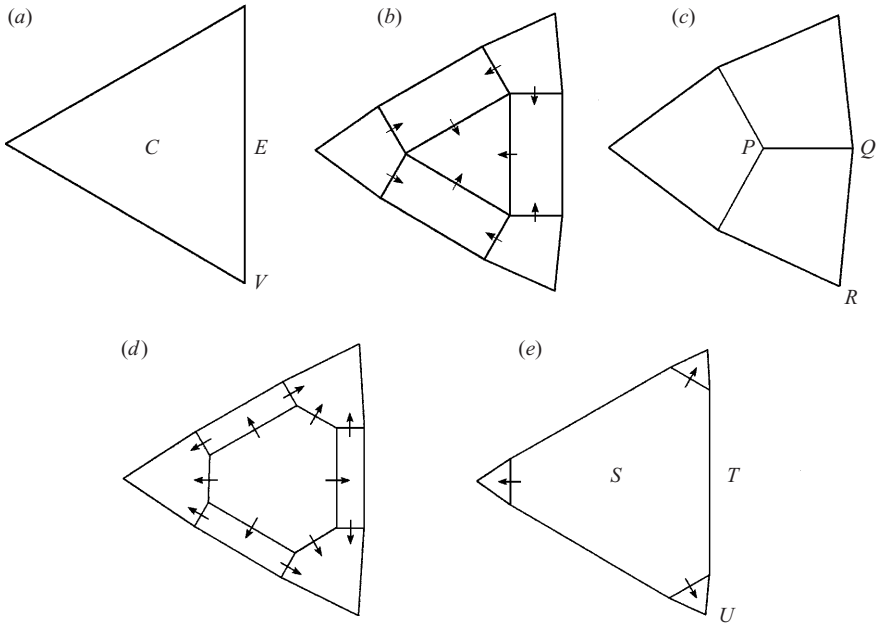


FIGURE 4. Top view of the successive shock surfaces in a converging channel corresponding to the construction in the cut planes shown in figure 3. (The contraction in scale is not shown in the figure.) The arrows indicate the direction of propagation of the shock-shocks.

the shock surface shown in figure 4(c) results. This configuration would correspond to the formation of a dodecahedron as described in figure 1 for the case when the convergence angle ϕ is 37.38°, or to regular polyhedra with 6 or 4 faces when ϕ equals 54.74° or 70.53°, respectively.

The condition for the incident shock to vanish at the point P shown in figure 4(c) can be worked out from the geometry of the shock-shock paths in figure 3 and (2.4) and (2.5) for the angles χ and ξ. The distance $|OQ|$ in figure 3 can be determined in two ways. Let R_1 and R_2 denote the distance $|OQ|$ according to the geometry in the planes OCE and OEV, respectively. A straightforward application of trigonometry gives

$$R_1 = \left(\frac{\tan\chi}{\tan\theta + \tan\chi}\right)|OE|, \quad R_2 = \left(\frac{\sec^2\psi\tan\xi}{\tan\psi + \tan\xi}\right)|OE|.$$

The values of R_1 and R_2 must be equal for the configuration in figure 4(c) to occur. The shock-shock formulas (2.4) and (2.5) give the angles χ and ξ implicitly in terms of θ and ψ, respectively, and in terms of the exponent n in the area–Mach number relation (2.3). The angles θ and ψ, in turn, are related to ϕ by the geometric formula (2.1) so that the ratio R_1/R_2 depends on ϕ and n alone. In figure 5, we plot the ratio R_1/R_2 as a function of ϕ for integer values of n between 1 and 7. As may be seen from the curves, there is a unique value of ϕ for a given value of n for which the ratio is 1 and the configuration in figure 4(c) occurs. The values of ϕ with $R_1/R_2 = 1$ range between 0 as $n \to 0$ and 70.53° as $n \to \infty$. The collapse of a strong shock in the shape of an icosahedron initially to a dodecahedron corresponds to the case $\phi = 37.38°$ and would occur when $n = 1.185$, and the collapse of a strong shock in the shape of an octahedron initially to a hexahedron corresponds to the case $\phi = 54.74°$ and would occur when $n = 4.269$. The limiting value of $\phi = 70.53°$ ($n \to \infty$) corresponds to the collapse of a strong shock in the shape of a regular tetrahedron initially.

https://doi.org/10.1017/S0022112001007170 Published online by Cambridge University Press

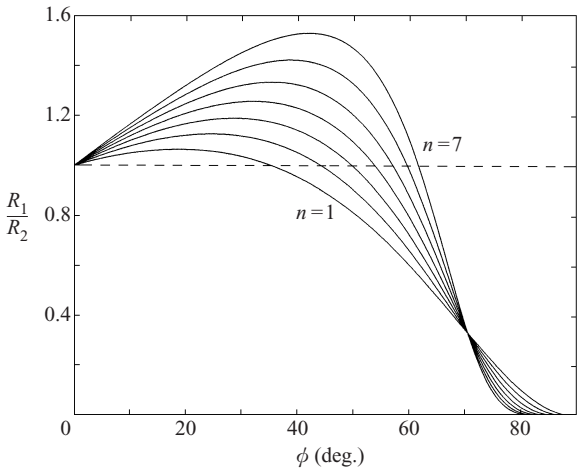


FIGURE 5. Ratio of distances R_1 and R_2 versus ϕ for integer values of n.

Assuming that ϕ and n are such that the evolution to the configuration in figure 4(c) occurs, the final step is to consider whether the shock returns to a planar shape. Each shock-shock edge, such as PQ, and the vertex at P opens up to form new Mach faces and corresponding shock-shocks as shown in figure 4(d). The angle of the new shock-shocks from P relative to the effective wall OP in the cut plane OCE is χ, and the angle of the shock-shock from the edge PQ from the effective wall OQ in the cut plane OEV is ξ as shown in figure 3. These angles depend only on ϕ and n, and are the same ones as those determined implicitly in (2.4) and (2.5) with σ and μ replaced by M_4/M_5 and M_3/M_4, respectively. The geometry of figure 3 is now completely determined, and we see that a return to a planar shock would occur if the path of shock-shocks from Q met at the point U so that the Mach stem at that point vanished. This condition, however, is not possible according to the geometry of figure 3 (excluding the limiting case $n \to \infty$) so that there is always a small Mach stem at U as shown in the figure. This configuration corresponds to the shock surface shown in figure 4(e).

The analysis of a converging shock whose initial shape takes the form of a regular polyhedron with 20, 8 or 4 faces has shown that the shock may evolve into the shape of a regular polyhedron with 12 or 6 faces at a later time depending on the value of n in the area–Mach number rule (excluding the limiting case $n \to \infty$). However, the analysis also shows that it is not possible for the shock to return in shape to its original regular polyhedral configuration (with reduced size). While it is possible to pursue the evolution of other (non-regular) polyhedral shock shapes analytically, we turn instead to a numerical approach which will be used to demonstrate that converging polyhedral shocks do evolve into repeating configurations that are more complex than the ones considered analytically above. In addition, the numerical method will be used to study the behaviour of converging spherical shocks subject to smooth initial perturbations.

3. Numerical method for three-dimensional shock propagation

In this section, we develop a numerical method which may be used to calculate the motion of a leading shock front in three space dimensions as determined by a

https://doi.org/10.1017/S0022112001007170 Published online by Cambridge University Press

solution of the equations of geometrical shock dynamics. The numerical approach is based on a finite-volume discretization of the conservation form of the equations of geometrical shock dynamics, and may be considered as an extension of the method developed in Schwendeman (1999) for shock propagation in two dimensions. Both methods are Godunov-type methods (Godunov 1959), and compute numerical fluxes based on the solution of a suitable Riemann problem. For the geometries considered here an unstructured grid based on triangular prism cells is convenient, in contrast to the methods discussed in Schwendeman (1993) and Schwendeman (1999) which use structured grids. It is also noted that the method developed here is a fixed-grid (Eulerian) method which has favourable stability and accuracy properties compared to the moving-grid (Lagrangian) method used in Schwendeman (1988).

3.1. *Governing equations and discretization*

The equations of geometrical shock dynamics in conservation form are

$$\nabla \cdot \left(\frac{M}{A} \nabla \alpha \right) = 0, \quad M = \frac{1}{|\nabla \alpha|}, \quad A = A(M), \tag{3.1}$$

where the shock position $\boldsymbol{x}$ at a time t is given by the surface $\alpha(\boldsymbol{x}) = a_0 t$ (for a uniform ambient sound speed a_0) and $A = A(M)$ is an assumed area–Mach number relation such as that given by (2.3) for strong shocks (see Whitham 1974). The partial differential equation for α in (3.1) is nonlinear and hyperbolic, assuming that $A'(M) < 0$, and describes disturbances in Mach number and shock-front normal that propagate along the shock surfaces, which evolve in the direction of $\nabla\alpha$. The object of the numerical method is to determine a discrete representation for $\alpha(\boldsymbol{x})$ throughout the region of interest so that the successive shock positions may then be determined by computing level surfaces of α.

Equations (3.1) are to be solved for α in a three-dimensional region Ω (such as the converging channel shown in figure 2). Let the surface S_0 denote the portion of the boundary of Ω on which the arrival time for the leading shock front and its Mach number are known. These data correspond to prescribing α and its normal derivative on S_0. For many problems, including the ones considered in this paper, the surface S_0 coincides with the shock surface at $t = 0$ so that $\alpha = 0$ on S_0, but this is not essential. For the purposes of our numerical method, we now introduce a one-parameter family of surfaces $S(\eta)$ that describes the region Ω for $0 \leqslant \eta \leqslant \eta_{\text{final}}$ with $S(0) = S_0$. The hyperbolic equation for α will be solved numerically by advancing the solution on the family of surfaces $S(\eta)$ for increasing values of the parameter η. It is noted that while η plays the role of time for the numerical method, it is not equal to the actual time t for a given shock front position in general, and the chosen surfaces $S(\eta)$ are not the shock front positions given by the level surfaces $\alpha(\boldsymbol{x}) = a_0 t$. The exact solution, in fact, evolves in the direction of $\nabla\alpha$ as mentioned before.

We may now define a grid Ω_h by the family of discrete surfaces $S_h(\eta)$, $0 \leqslant \eta \leqslant \eta_{\text{final}}$, where h denotes a measure of the grid spacing. For the geometries considered in this paper, it is convenient to describe $S_h(\eta)$ by a set of triangular elements as shown in figure 6, where $\boldsymbol{x}_i(\eta)$, $i = 1, \ldots, N_v$, $0 \leqslant \eta \leqslant \eta_{\text{final}}$, define the paths of the vertices of the triangular elements. We also define $\tilde{\alpha}_k(\eta)$, $k = 1, \ldots, N_e$, to be a set of discrete approximations for α on the surface $S_h(\eta)$. These discrete values are located at edge centres as shown in figure 6. Lastly, we define $\tilde{F}_j(\eta)$, $j = 1, \ldots, N_c$, to be a set of discrete approximations for $(M/A)\nabla\alpha \cdot \boldsymbol{n}$ on the surface $S_h(\eta)$ located at triangle centres, where the unit surface normal $\boldsymbol{n}$ points in the direction of increasing η.

Let us consider an individual triangular element on the surface $S_h(\eta)$ with centre

https://doi.org/10.1017/S0022112001007170 Published online by Cambridge University Press

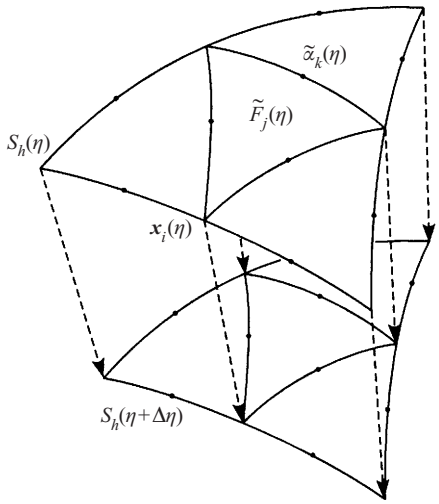


FIGURE 6. A small portion of the unstructured grid on surfaces $S_h(\eta)$ and $S_h(\eta + \Delta\eta)$.

index $j = j_0$, say, and corresponding edge indices $k = k_1$, k_2, and k_3. The triangular element maps out a triangular prism over an increment $\Delta\eta$ in the parameter η. An application of the divergence theorem to the equation for α in (3.1) for this prism suggests the conservative discretization

$$\tilde{F}_{j_0}(\eta + \Delta\eta)a_{j_0}(\eta + \Delta\eta) = \tilde{F}_{j_0}(\eta)a_{j_0}(\eta) - \sum_{p=1}^{3} \tilde{G}_{k_p}(\eta)b_{k_p}(\eta), \tag{3.2}$$

where a_{j_0} is the surface area of the triangular element, b_{k_p} is the surface area of the pth side of the prism, and $\tilde{G}_{k_p}$ is a discrete approximation for $(M/A)\nabla\alpha \cdot \boldsymbol{v}_{k_p}$ on the pth side with outward unit normal $\boldsymbol{v}_{k_p}$. The approximations for α on the edges are advanced using

$$\tilde{\alpha}_{k_p}(\eta + \Delta\eta) = \tilde{\alpha}_{k_p}(\eta) + \tilde{u}_{k_p}(\eta)c_{k_p}(\eta), \quad p = 1,\ 2 \text{ and } 3, \tag{3.3}$$

where c_{k_p} is the distance from the pth edge centre at η to that at $\eta + \Delta\eta$, and $\tilde{u}_{k_p}$ is a discrete approximation for $\nabla\alpha \cdot \boldsymbol{\tau}_{k_p}$ on the pth side with unit tangent vector $\boldsymbol{\tau}_{k_p}$ pointing in the direction of the path of the edge centres. The surface areas a_{j_0} and b_{k_p} and the distance c_{k_p} are computed easily from the geometry of the grid and a given choice for the increment $\Delta\eta$. Values for $\tilde{G}_{k_p}$ and $\tilde{u}_{k_p}$ are obtained from the solution of a Riemann problem as will be discussed in § 3.2 below. Assuming that these values can be found, (3.2) and (3.3) provide formulas for advancing the discrete sets $\{\tilde{F}_j\}$ and $\{\tilde{\alpha}_k\}$, respectively, from $S_h(\eta)$ to $S_h(\eta + \Delta\eta)$. Starting values for $\{\tilde{F}_j\}$ and $\{\tilde{\alpha}_k\}$ are known on $S_h(0)$ from the incoming shock data on the surface S_0.

Before proceeding to a discussion of the Riemann problem and the calculation of $\tilde{G}_{k_p}$ and $\tilde{u}_{k_p}$, a constraint on the numerical method is noted. The constraint may be seen in the problem of computing components of $\nabla\alpha$ from the data $\{\tilde{F}_j\}$ and $\{\tilde{\alpha}_k\}$. These values are needed to compute the shock Mach number and to provide left and right states for the Riemann problem. For example, let us consider again the triangular element j_0 with edges k_1, k_2 and k_3, and suppose u_0 is the component of $\nabla\alpha$ in the normal direction $\boldsymbol{n}_{j_0}$ and v_0 and w_0 are components of $\nabla\alpha$ in the tangent plane of the surface. Second-order-accurate approximations for v_0 and w_0 may be

https://doi.org/10.1017/S0022112001007170 Published online by Cambridge University Press

computed from the edge values for α by solving the linear equations

$$\boldsymbol{h}_p \cdot (v_0 \boldsymbol{e}_v + w_0 \boldsymbol{e}_w) = \tilde{\alpha}_{k_p} - \tilde{\alpha}_{k_1}, \quad p = 2 \text{ and } 3,$$

where $\boldsymbol{h}_p$ is the vector from the edge centre k_1 to the edge centre k_p, and $\boldsymbol{e}_v$ and $\boldsymbol{e}_w$ are unit vectors in the tangent plane of the surface corresponding to the (orthogonal) directions of the components v_0 and w_0, respectively. The definitions of $\tilde{F}_{j_0}$ and M_0 provide nonlinear equations for u_0:

$$\tilde{F}_{j_0} = \left(\frac{M_0}{A(M_0)}\right) u_0, \quad M_0 = (u_0^2 + v_0^2 + w_0^2)^{-1/2},$$

but these equations are not solvable for all choices of v_0, w_0, and $\tilde{F}_{j_0}$. For the area–Mach number relation (2.3), solutions exist for

$$\tilde{F}_{j_0} < \frac{1}{\sqrt{n+1}} \left[\frac{n+1}{n}(v_0^2 + w_0^2)\right]^{-n/2} \quad \text{and} \quad u_0 > \left(\frac{v_0^2 + w_0^2}{n}\right)^{1/2}. \tag{3.4}$$

The latter inequality is equivalent to the geometric constraint that the characteristic cone about $\nabla\alpha$ cannot become tangent to the grid surface $S_h(\eta)$. This limits the angle between the shock surfaces $\alpha(\boldsymbol{x}) = a_0 t$ as determined by a solution of (3.1) and the chosen family of surfaces $S(\eta)$ for the numerical method. This constraint is analogous to the one discussed previously in Schwendeman (1999). The implication of the constraint for the problems of interest for this paper will be discussed in § 4.

3.2. *The Riemann problem for geometrical shock dynamics*

A Riemann problem is solved numerically in the neighbourhood of each face of the prism elements in order to obtain approximations for $\tilde{G}_k$ and $\tilde{u}_k$ needed in (3.2) and (3.3) to advance $\tilde{F}_j$ and $\tilde{\alpha}_k$, respectively, on the grid. This approach is similar to the one used in Schwendeman (1999) for two-dimensional shock propagation. For geometrical shock dynamics, a suitable Riemann problem for a system of first-order hyperbolic partial differential equations, equivalent to the second-order scalar equation for α in (3.1), may be introduced and solved for the components of $\nabla\alpha$. The solution consists of intervals of constant $\nabla\alpha$ separated by shock-shocks or shock-expansions. (The term 'shock-expansion' used in the present discussion refers to smooth, expansion-type solutions of the equations.) For the two-dimensional case, formulas for these transitions are available in Whitham (1974). The analogous formulas for the three-dimensional case are new and are discussed below. A method of iteration involving the formulas for shock-shocks and shock-expansions is used to solve the Riemann problem numerically and determine values for $\tilde{G}_k$ and $\tilde{u}_k$.

Let us consider an orthogonal coordinate system (x, y, z) in the neighbourhood of a prism face, where x measures distance along the face in the direction of increasing η, y measures distance normal to the face, and z measures distance along the face in the cross-flow direction (perpendicular to the x-direction). Suppose further that $\boldsymbol{u} = (u, v, w)$ are the components of $\nabla\alpha$ in the (x, y, z) directions, respectively. In this local system, the governing equations (3.1) become

$$\frac{\partial}{\partial x}\left(\frac{M}{A(M)}u\right) + \frac{\partial}{\partial y}\left(\frac{M}{A(M)}v\right) + \frac{\partial}{\partial z}\left(\frac{M}{A(M)}w\right) = 0, \tag{3.5}$$

and $M = (u^2 + v^2 + w^2)^{-1/2}$, together with the identities

$$\frac{\partial v}{\partial x} - \frac{\partial u}{\partial y} = 0, \quad \frac{\partial w}{\partial x} - \frac{\partial u}{\partial z} = 0. \tag{3.6}$$

https://doi.org/10.1017/S0022112001007170 Published online by Cambridge University Press

For the purposes of the numerical method, we are interested in solutions of (3.5) and (3.6), depending on (x, y) only, subject to piecewise constant data at $x = 0$. This Riemann problem is

$$\left.\begin{aligned} \frac{\partial}{\partial x}F(\boldsymbol{u}) + \frac{\partial}{\partial y}G(\boldsymbol{u}) &= 0, \\ \frac{\partial v}{\partial x} - \frac{\partial u}{\partial y} &= 0, \\ \frac{\partial w}{\partial x} &= 0, \end{aligned}\right\} \quad x > 0, \quad |y| < \infty, \tag{3.7}$$

with

$$F(\boldsymbol{u}) = \frac{Mu}{A(M)}, \quad G(\boldsymbol{u}) = \frac{Mv}{A(M)}, \tag{3.8}$$

and

$$\boldsymbol{u}(0, y) = \begin{cases} \boldsymbol{u}_\ell & \text{for } y < 0, \\ \boldsymbol{u}_r & \text{for } y > 0, \end{cases}$$

where the data $(\boldsymbol{u}_\ell, \boldsymbol{u}_r)$ are obtained from the components of $\nabla\alpha$ belonging to neighbouring triangular grid cells. If the prism face coincides with a wall boundary of Ω_h, then the reflection condition $(u_\ell, v_\ell, w_\ell) = (u_r, -v_r, w_r)$ is used to determine the ghost state outside the boundary.

We note immediately that $w(x, y) = w(0, y)$ from the third equation in (3.7) so that the solution of the Riemann problem develops for $x > 0$ with a known constant value for the cross-flow component of $\nabla\alpha$ on either side of $y = 0$. The third equation may now be discarded and solutions for the remaining two equations sought with $w =$ constant on either side of $y = 0$. The jump conditions for shock-shocks (to be discussed below) shows that G and u are continuous at $y = 0$ for $x > 0$, and these values are the ones used for $\tilde{G}_k$ and $\tilde{u}_k$ in (3.2) and (3.3), respectively.

Shock-shock solutions of (3.7) from an arbitrary state $\boldsymbol{u}_1$ to a state $\boldsymbol{u}_2$ satisfy the jump conditions

$$U[F(\boldsymbol{u}_2) - F(\boldsymbol{u}_1)] = G(\boldsymbol{u}_2) - G(\boldsymbol{u}_1), \quad U[v_2 - v_1] = -u_2 + u_1, \quad U[w_2 - w_1] = 0,$$

where $U = \mathrm{d}y/\mathrm{d}x$ is the slope of the path of discontinuity. One family of solutions occurs when $U = 0$. For this case, the jump in w is arbitrary and u and $G(\boldsymbol{u})$ are continuous. This is the jump (a contact discontinuity) at $y = 0$ as mentioned above. The other family of solutions occurs when $U \neq 0$. For this case, $w = w_1 = w_2$, $U = -(u_2 - u_1)/(v_2 - v_1)$, and

$$-(u_2 - u_1)[F(\boldsymbol{u}_2) - F(\boldsymbol{u}_1)] = (v_2 - v_1)[G(\boldsymbol{u}_2) - G(\boldsymbol{u}_1)].$$

This latter equation can be rewritten in the form

$$\tan(\vartheta_2 - \vartheta_1) = -\frac{[(r_2^2 - r_1^2)(A_2^2 M_1^2 r_1^2 - A_1^2 M_2^2 r_2^2)]^{1/2}}{A_2 M_1 r_1^2 + A_1 M_2 r_2^2} \tag{3.9}$$

using the definitions of F and G in (3.8) and introducing the polar coordinates $u = r\cos\vartheta$ and $v = r\sin\vartheta$. There is a choice of sign for the square root in (3.9). Assuming that $\boldsymbol{u}_1$ lies to the left of $\boldsymbol{u}_2$, we take the minus sign since ϑ decreases with increasing y for a solution in which the shock front propagates into the shock-shock. (This choice of sign plays the role of satisfying an entropy condition.) It is also noted that (3.9) reduces to the usual formula for shock-shocks when $w = 0$.

Shock-expansion solutions of (3.7) may be found by first writing the equations in

https://doi.org/10.1017/S0022112001007170 Published online by Cambridge University Press

characteristic form. The third equation is already in characteristic form, while a linear combination of the first and second equations in (3.7) gives

$$mF_u(\boldsymbol{u})\frac{\mathrm{d}u}{\mathrm{d}x} + G_v(\boldsymbol{u})\frac{\mathrm{d}v}{\mathrm{d}x} = 0, \tag{3.10}$$

which holds on characteristics with slope $\mathrm{d}y/\mathrm{d}x = m$, where m is a root of the quadratic

$$m^2F_u(\boldsymbol{u}) - m(F_v(\boldsymbol{u}) + G_u(\boldsymbol{u})) + G_v(\boldsymbol{u}) = 0. \tag{3.11}$$

We now eliminate m from equations (3.10) and (3.11), and use the definitions of F and G in (3.8) to obtain the differential form

$$(u^2 + v^2 + w^2)(\mathrm{d}u^2 + \mathrm{d}v^2) = (1 + \beta^2)(u\mathrm{d}u + v\mathrm{d}v)^2, \quad \beta^2 = -\frac{MA'}{A}, \tag{3.12}$$

which holds on the two families of characteristics. Again, it is convenient to use polar coordinates, $u = r\cos\vartheta$, $v = r\sin\vartheta$, so that the differential form in (3.12) becomes

$$\frac{\mathrm{d}\vartheta}{\mathrm{d}r} = \pm\left[\frac{\beta^2r^2 - w^2}{r^2(r^2 + w^2)}\right]^{1/2}. \tag{3.13}$$

For the strong shock case, $\beta^2 = n$ and (3.13) may be integrated (keeping in mind that w is constant) to give

$$\vartheta_2 - \vartheta_1 = \pm[P(r_2, w) - P(r_1, w)], \tag{3.14}$$

for a shock-expansion transition from a state (r_1, ϑ_1, w) to (r_2, ϑ_2, w). The function $P(r, w)$ in (3.14) plays the role of a Prandtl–Meyer function, and is given by

$$P(r, w) = \frac{\sqrt{n}}{2}\ln\left(r^2 + \frac{n-1}{2n}w^2 + \frac{pq}{\sqrt{n}}\right) - \frac{1}{2}\arctan\left(\frac{p^2 - q^2}{2pq}\right),$$

where $p^2 = nr^2 - w^2$ and $q^2 = r^2 + w^2$. The choice of sign in (3.14) reflects the two families of shock-expansion solutions and can be made following the condition that ϑ increases with increasing y for both families.

We now have the necessary formulas available to complete the solution of the Riemann problem. The solution consists of constant states in $\boldsymbol{u}$ separated by shock-shocks or shock-expansions given by (3.9) and (3.14), respectively, with $w = w_\ell$ or w_r, and a contact discontinuity at $y = 0$ across which w jumps from w_ℓ to w_r and G and u are continuous. A numerical method of iteration is used to determine the solution and in particular the values of G and u. The iteration begins with values for each constant state given by a linearization of the equations. Newton's method is used to update the values for $\boldsymbol{u}$ iteratively until the values for G and u on $y = 0$ converge to within a specified tolerance (taken to be 10^{-6}). These values become $\tilde{G}_k$ and $\tilde{u}_k$ in (3.2) and (3.3), respectively.

The numerical method described in §§ 3.1 and 3.2, essentially a Godunov method, is first-order accurate if the left and right states for the Riemann problem at each face are taken from the discrete data at neighbouring grid cells alone. Higher-order methods (for smooth regions of the solution) could be obtained by making corrections to the left and right states based on discrete approximations for the gradient of $\boldsymbol{u}$ (see Schwendeman 1999, for example). This is not done here because of the added numerical cost, mainly, and because for many of the problems computed the solutions contain regions of uniform (or nearly uniform) $\boldsymbol{u}$ separated by shock-shocks. We also note that approximate Riemann solvers could be used but since the problems of interest involve collisions of shock-shocks an exact Riemann solver is preferred.

https://doi.org/10.1017/S0022112001007170 Published online by Cambridge University Press

Finally, we note that the increment in the parameter η is computed according to a CFL stability condition:

$$\Delta\eta = C \min_{1\leqslant k\leqslant N_e} \left\{ \frac{L_k}{\bar{m}_k (\mathrm{d}s/\mathrm{d}\eta)_k} \right\},$$

where L_k is the minimum distance between the kth edge centre and the two opposing vertices belonging the left and right cells, $\bar{m}_k$ is the maximum in absolute value of the two slopes of the characteristics given by the quadratic in (3.11), and $(\mathrm{d}s/\mathrm{d}\eta)_k$ is the rate of increase of distance in the x-direction from the kth edge centre with η. The constant C is taken to be 0.8 for all calculations.

4. Shock propagation in a converging channel

We now return to the problem of shock propagation in a converging channel with triangular cross-section. The geometry of the channel, as shown in figure 2, is described by the convergence angle ϕ, and while the angles 70.53°, 54.74° and 37.38° are relevant for the problem of a converging shock whose initial shape takes the form of regular polyhedra with 4, 8 and 20 faces, respectively, we need not be restricted to these angles alone. In fact, our numerical calculations suggest that the general behaviour of the converging shock is independent of the choice for ϕ. Calculations have been made for a wide range of angles and in all cases considered, it is found that an initially planar shock evolves into repeating configurations whose Mach numbers increase with decreasing radius according to the same behaviour as for a converging spherical shock. These repeating configurations appear to be the stable ones for the converging channel geometry.

In order to implement the numerical method for the converging channel geometry, we need to make a choice for the family of surfaces $S(\eta)$ on which the solution of the governing equations (3.1) will be computed. A simple choice would be a family of planar surfaces with normals parallel to the centreline OC evolving from the initial shock surface when $\eta = 0$ towards the convergence point O. This choice is adequate for relatively small values of ϕ (less than about 30°) but is not the best choice for larger angles. For larger values of ϕ, the angle at which the shock is turned by the channel walls is greater so that the angle between $\nabla\alpha$ and the centreline becomes large, and the constraint given by the inequalities in (3.4) is reached ultimately. A better choice for $S(\eta)$ begins with a planar surface at $\eta = 0$, so that $S(0)$ coincides with the initial shock surface for convenience as before, but then evolves into a family of spherical surfaces converging towards O. This choice is used for the calculations presented in this section and is adequate for values of ϕ to about 45°. Solutions for converging channels with larger values of ϕ are difficult to calculate using a family of smooth surfaces due to the large jump in the shock-front normals created by Mach reflections at the channel walls initially and later in the interior.

Let us concentrate first on the behaviour of a shock propagating in a converging channel with $\phi = 20°$. Initially, the shock is planar with Mach number equal to 2, and it is located at the inlet to the channel where $|OV| = 1$. A value of $n = 5.0743$ is used in the area–Mach relation (2.3) corresponding to strong shock propagation in air. The parameters N_c, N_e and N_v which describe the resolution of the grid are 65 536, 98 688 and 33 153, respectively. Figure 7 shows shock surfaces in the converging channel for (early) times between 0.118 and 0.196 (assuming a unit sound speed for the gas ahead of the shock). The surfaces in the figure are shaded according to the local shock Mach number with the lighter shades corresponding to higher Mach numbers (larger

https://doi.org/10.1017/S0022112001007170 Published online by Cambridge University Press

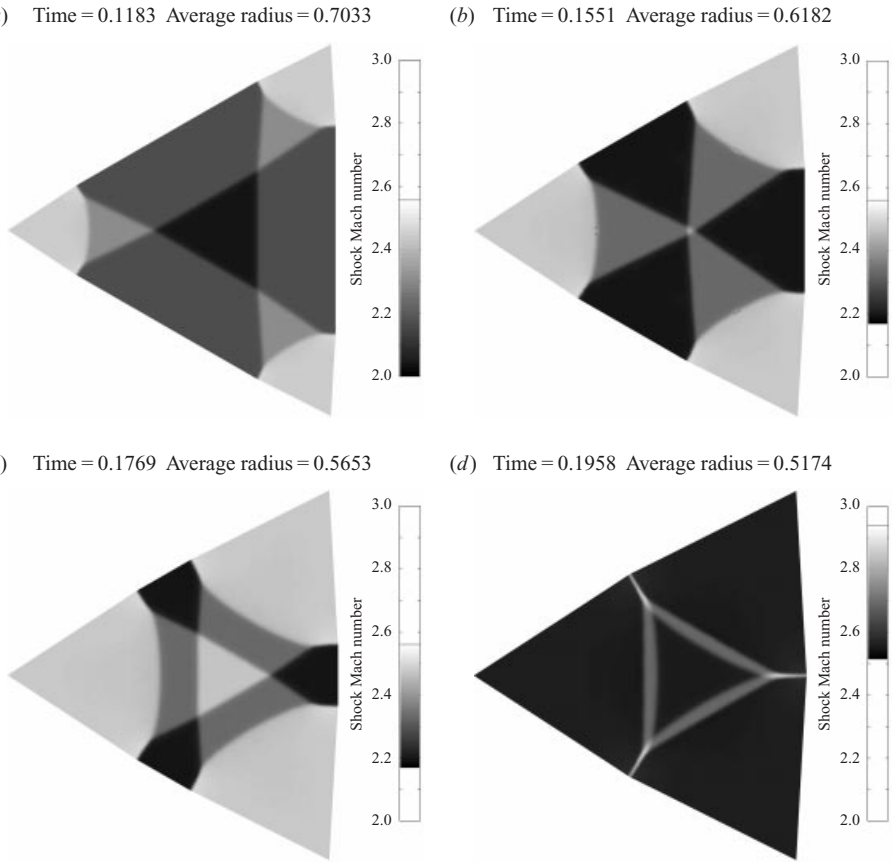


FIGURE 7. Shock surfaces in a converging channel with $\phi = 20°$: early behaviour.

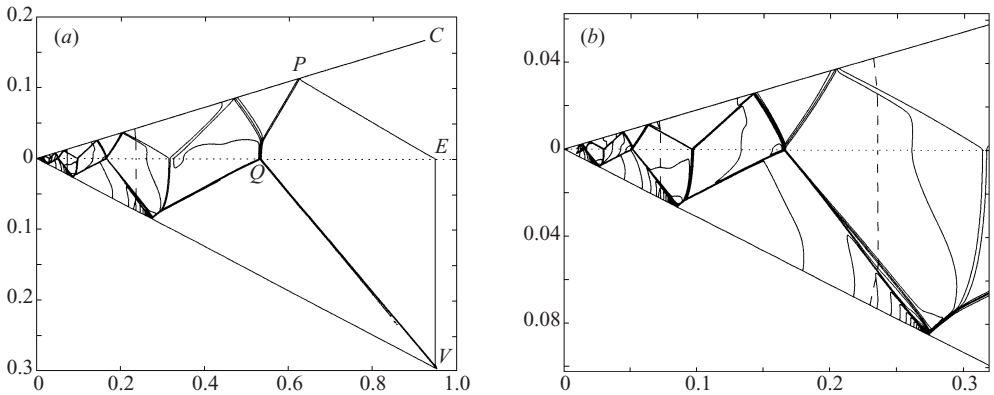


FIGURE 8. Contours of Mach number in the planes OCE and OEV for shock propagation in a converging channel with $\phi = 20°$.

shock strengths). The grey-scale bar to the right of each plot gives the range of Mach numbers for each surface. As the shock propagates, its size decreases but each surface is scaled to its initial size for clarity. The actual size of each shock surface is indicated by its average radial distance from the convergence point as listed above each plot. In

https://doi.org/10.1017/S0022112001007170 Published online by Cambridge University Press

order to interpret the behaviour of these shock surfaces, it is convenient to consider contours of the shock Mach number in the cut planes OCE and OEV as shown in Figure 8(a). The surface in figure 7(a) gives a representative view of the shock after its initial interaction with the channel walls. The dark central region of the surface is the incident planar shock from C and the lighter shaded regions surrounding it are the Mach stems formed from the Mach reflections at E and at V as labelled in figure 8(a). For this choice of ϕ and n, the rate of advance of the shock-shock from E is greater than that from V so that the incident shock collapses to a point (as shown in figure 7b) before the Mach stem from E is consumed by the Mach stem from V. This corresponds to $R_1/R_2 > 1$ in figure 5 and is in contrast to the behaviour of the shock surfaces for the special case $R_1/R_2 = 1$ as discussed previously and shown in figure 4. After the collapse of the incident shock, a new shock is formed along the centreline at P and grows to become the surface shown in figure 7(c). This growing shock eventually meets the Mach stems from V (at the point labelled Q in figure 8a) to form the shock surface shown in figure 7(d).

The later-time behaviour of the shock surfaces may be interpreted with the aid of figure 8(b), which shows an enlarged view of contours of shock Mach numbers near the convergence point. This plot gives a first indication of a repeating behaviour of the propagating shock. A portion of the plot that repeats is marked by the region between the dashed curves to the right and the left representing the intersection of the cut planes and the shock surfaces at $t = 0.292$ and 0.331, respectively. Upon close inspection of the figure, it may be seen that this section scales down and repeats as the shock propagates towards O. Further evidence of this repeating behaviour may be seen in the sequence of 12 shock surfaces shown in figure 9. The first shock surface in the sequence corresponds to the dashed curve on the right in figure 8(b) while the last shock corresponds to the dashed curve on the left. The behaviour of the shock may be followed in time through the sequence by using the general rule that lighter shaded regions having larger shock strength consume darker regions with lower shock strength. By the end of the sequence, it is noted that the first shock surface in the sequence has re-formed, but with a larger overall strength and a reduced size as indicated by its average radial distance from O. The shock surfaces in the sequence are more complicated than the ones considered in § 2, and they have developed non-planar pieces so that an exact solution would be difficult to construct analytically.

As the shock converges, its Mach number increases, and it is interesting to compare the rate of increase with that given by a converging spherical shock. In the latter case, the increase in Mach number with decreasing radius can be worked out using the area–Mach number relation. The ray-tube area A for a spherical shock is proportional to r^2, where r is the radius, which gives

$$M \propto r^{-2/n}$$

using (2.3) for strong shocks. For the case of an initially planar shock propagating in a converging channel, the increase in Mach number with decreasing radius may be considered by following the behaviour along rays from the initial shock surface towards the convergence point. In figure 10, we show log-log plots of the shock Mach number along rays from the points C, E and V as a function of r for the cases $\phi = 20°$, $\phi = 30°$ and $\phi = 37.38°$. The latter case corresponds to a converging shock whose initial shape is an icosahedron. The sharp increases in Mach numbers observed in the plots are caused by Mach reflections at walls or by shock-shock collisions (shock focusing). The most extreme behaviour is seen along the ray from V. The dashed lines in the plots have slope equal to $-2/n$ and they are in excellent agreement

https://doi.org/10.1017/S0022112001007170 Published online by Cambridge University Press

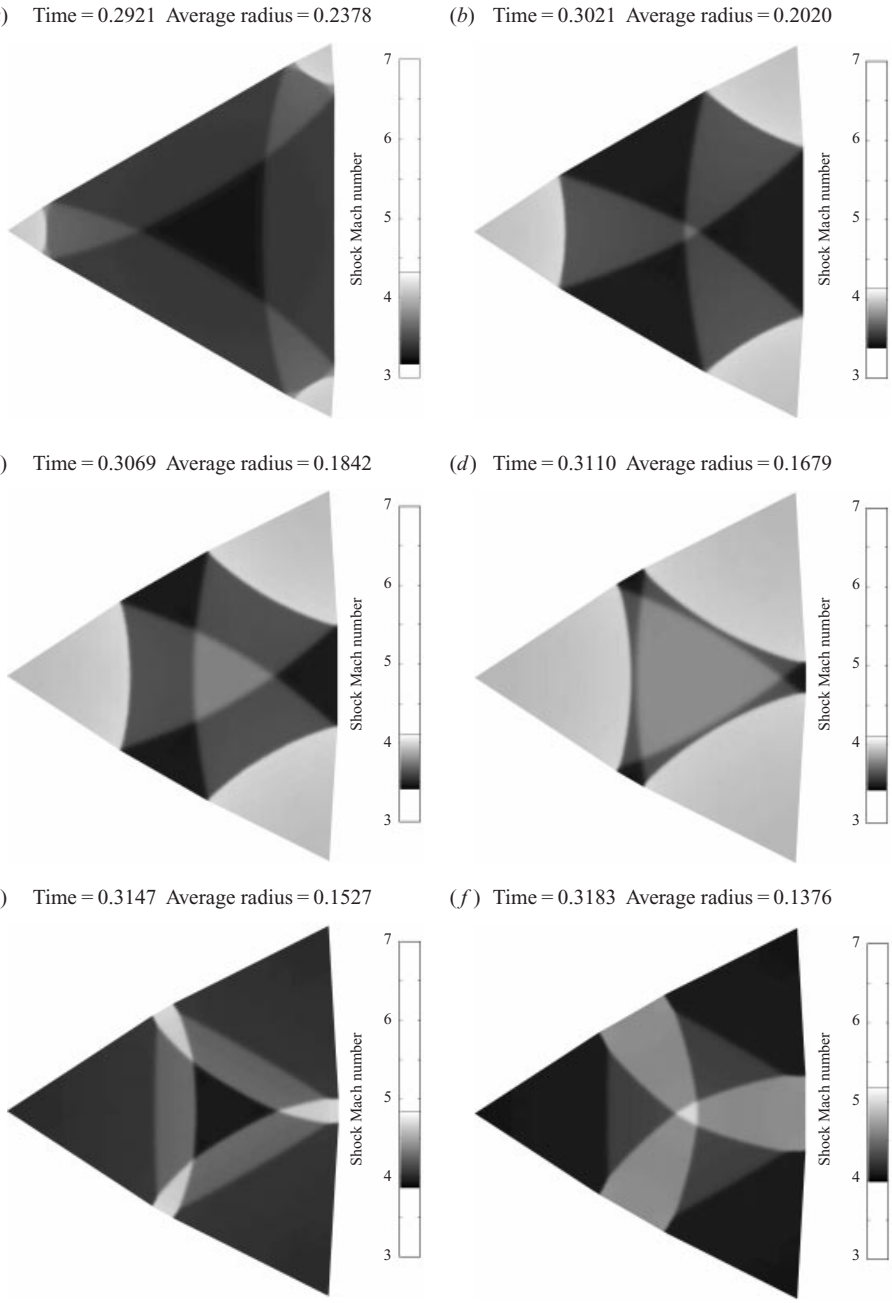


FIGURE 9 (*a–f*). For caption see facing page.

with the behaviour of the local extrema in Mach number along the ray from V. If we label the Mach number and radius at local maxima, say, as M_p and r_p, respectively, then it is evident from the plots that

$$M_p \propto r_p^{-2/n}$$

so that the increase in Mach number for each step of the repeating sequence follows

https://doi.org/10.1017/S0022112001007170 Published online by Cambridge University Press

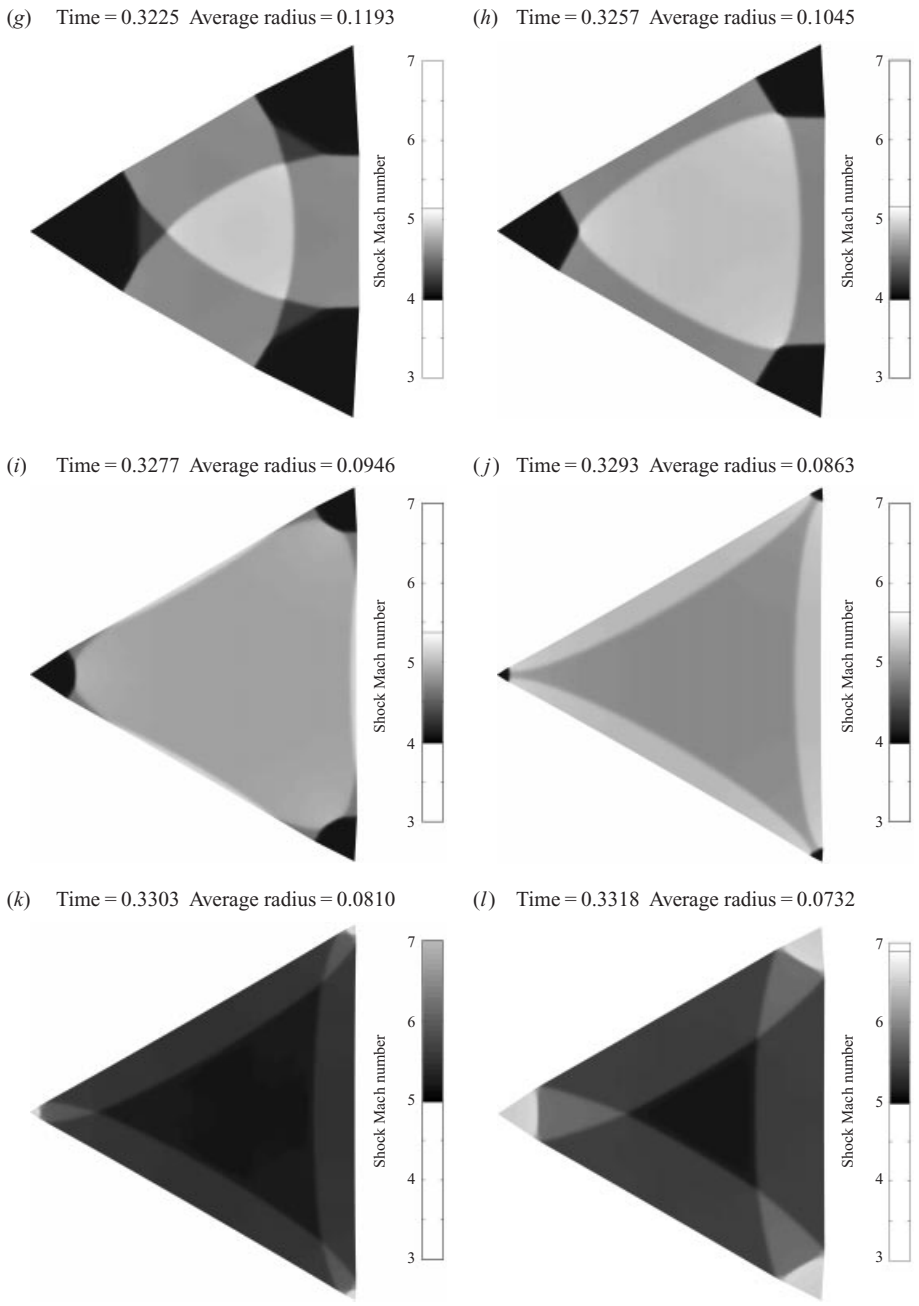


FIGURE 9 (*g–l*). Shock surfaces in a converging channel with $\phi = 20°$: repeating behaviour.

the same behaviour as that for a converging spherical shock independent of the choice of ϕ.

The repeating behaviour observed here is analogous to that found in Schwendeman & Whitham (1987) for converging cylindrical shocks. For the two-dimensional case, an exact solution was found for converging shocks whose initial shape takes the form of regular polygons. As the shock collapses the initial shape reforms repeatedly and

https://doi.org/10.1017/S0022112001007170 Published online by Cambridge University Press

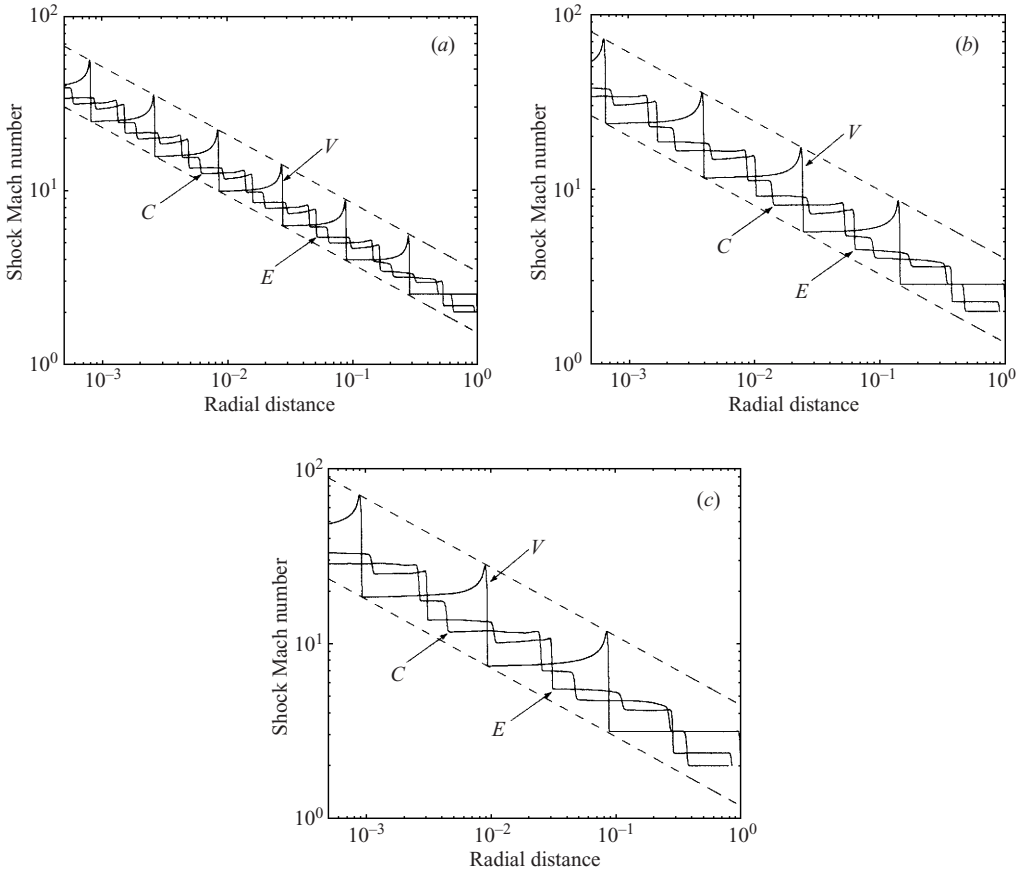


FIGURE 10. Behaviour of the shock Mach numbers along rays from the points V, E and C for (*a*) $\phi = 20°$, (*b*) $\phi = 30°$ and (*c*) $\phi = 37.38°$.

the increase in the shock Mach number with r at each step follows the same formula as for a converging circular shock independent of the number of sides of the polygon. There are effective walls implied by the symmetry of the initial polygon so that the exact solution may be reinterpreted as shock propagation in a converging wedge with convergence angle φ. The geometry of the polygon implies $\varphi = 2\pi/N$, where $N \geqslant 3$ is an integer, but we need not be restricted to these angles for the wedge problem and may consider any angle on $(0, \pi)$. The result would be the same. An initially plane shock re-forms at successive intervals as it propagates in the converging wedge independent of the choice for φ. We conclude that there is no essential difference between the two-dimensional case and three-dimensional case considered here, except that the initial planar shock does not re-form in the repeating sequence for the three-dimensional case and the shock surfaces are more complicated. Thus, our numerical calculations suggest that the stability result implied by the exact solution for the two-dimensional case carries over to the three-dimensional case as well.

5. Converging spherical shocks

The behaviour of converging spherical shocks subject to smooth perturbations in their initial strength may be considered using the numerical method discussed in § 3.

https://doi.org/10.1017/S0022112001007170 Published online by Cambridge University Press

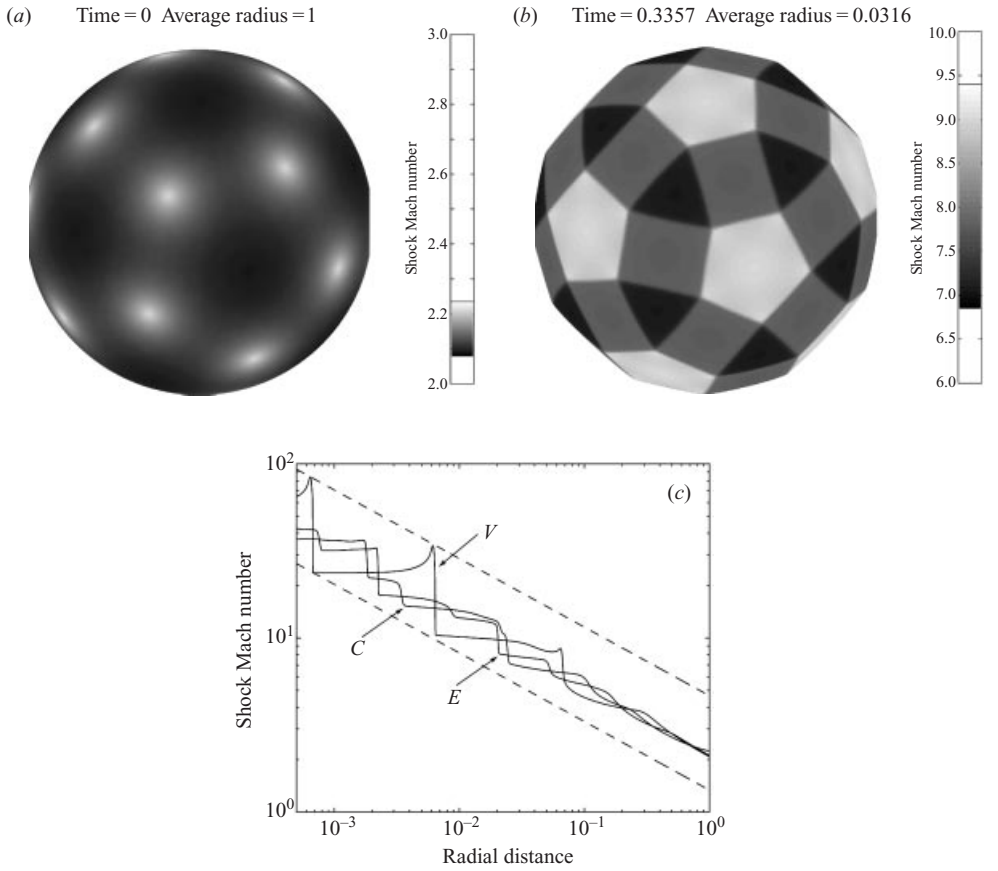


FIGURE 11. Converging spherical shock subject to smooth symmetric perturbation: (*a*) shock surface at $t = 0$, (*b*) shock surface at $t = 0.3357$, and (*c*) shock Mach numbers along rays.

For this case, the initial shock surface is assumed to be spherical, and the equations are solved numerically on a family of spherical surfaces $S(\eta)$ with decreasing radius, $r = \mathrm{e}^{-\eta}$, $0 < \eta < \eta_{\text{final}}$. The initial strength of the shock is described by a specified Mach number distribution which is taken to be

$$M(\boldsymbol{x}) = M_0 \left\{ 1 + \sum_{i=1}^{m} \epsilon_i [\exp(-s_i \phi_i(\boldsymbol{x})) + \exp(-s_i(\pi - \phi_i(\boldsymbol{x})))] \right\}, \tag{5.1}$$

where M_0 is a constant (unperturbed) Mach number, m is one half of the number of smooth 'bumps' in the initial distribution, ϵ_i and s_i give the magnitude and spread of the ith bump, respectively, and $\phi_i(\boldsymbol{x}) \in [0, \pi]$ is the angle between the position vector $\boldsymbol{x}$ on the surface of the initial spherical shock and a chosen vector $\boldsymbol{x}_i$ for the centre of the ith bump. The form of the perturbation given in (5.1) includes a reflectional symmetry about the origin so that the point of convergence is unchanged from the unperturbed case. Thus, the chosen family of surfaces $S(\eta)$ remains a suitable choice for the numerical integration as the shock collapses.

We consider first a case in which the initial perturbation has the same symmetry as that for a converging shock whose initial shape is an icosahedron. For this case, we set $m = 10$, $\epsilon_i = 0.1$ and $s_i = 4$ for $i = 1, \ldots, 10$, and take $\{\boldsymbol{x}_i\}$ to be the

https://doi.org/10.1017/S0022112001007170 Published online by Cambridge University Press

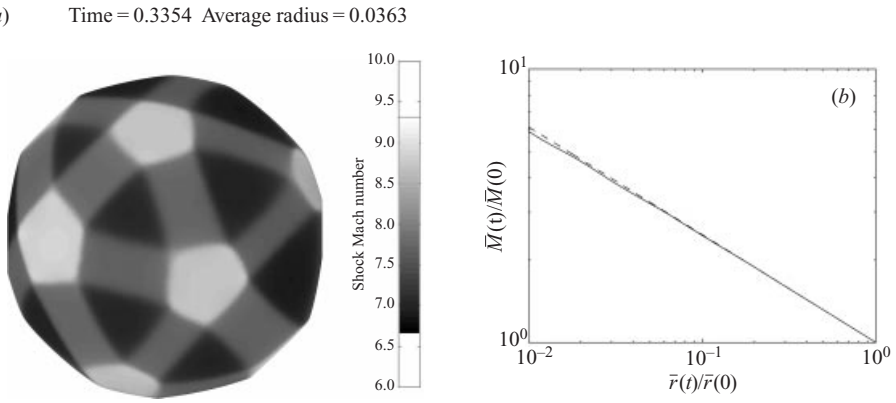


FIGURE 12. Converging spherical shock subject to a smooth asymmetric perturbation: (*a*) shock surface at $t = 0.3354$ and (*b*) average shock Mach number versus average radius.

positions of the 10 face centres of the polyhedron in the upper half-hemisphere. (The reflectional symmetry in (5.1) gives the corresponding perturbations in the lower half-hemisphere.) Figure 11(*a*) shows the initial shock surface with the prescribed distribution of smooth bumps in Mach number indicated by the lighter shaded spots on the spherical surface. As the shock collapses, the smooth perturbations grow and the shock surface develops (nearly) planar pieces connected by shock-shocks. A representative view of this later-time behaviour is given by the shock surface shown in figure 11(*b*). The behaviour of the shock Mach number along rays from points on the initial surface corresponding to the points C, E and V for the polyhedron is shown in figure 11(*c*). In this plot, it is clear that the smooth perturbation evolves into the repeating behaviour discussed earlier for the converging channel. This plot provides a strong indication that the repeating solution is the stable one for initial perturbations that possess the symmetry of a regular polyhedron.

As a last case, we consider the behaviour of a converging spherical shock subject to a smooth perturbation without symmetry, except for the reflectional symmetry built into (5.1). This may be done by choosing arbitrary values for m, $\{\epsilon_i\}$, $\{s_i\}$ and $\{\boldsymbol{x}_i\}$ in (5.1), and of course there are many possibilities from which to choose. The aim here is not to give a full picture of all possibilities, but rather to simply indicate a trend in the behaviour. For this purpose, we choose m, $\{s_i\}$ and $\{\boldsymbol{x}_i\}$ as in the symmetric case, but now take random values for $\{\epsilon_i\}$ on the interval $[0.0975, 0.125]$. For this choice, the very early behaviour is close to that observed in the symmetric case, but the symmetry is broken so that the repeating behaviour is not observed at later times. There is, however, still a trend towards shock surfaces composed of nearly planar pieces, similar to that reported in Schwendeman (1993), and this is seen in the sample shock surface shown in figure 12(*a*). In order to examine the behaviour of the Mach number of the converging shock, we compute a discrete approximation to an average Mach number defined by

$$\bar{M}(t) = \frac{1}{\sigma(t)} \int M \, \mathrm{d}\sigma, \quad M = \frac{1}{|\nabla \alpha|},$$

where the integral is taken over a shock surface $\alpha(\boldsymbol{x}) = a_0 t$ for a given time t, and $\sigma(t)$ is the surface area of the shock at t. In figure 12(*b*) we plot $\bar{M}(t)/\bar{M}(0)$ versus $\bar{r}(t) = (\sigma(t)/\sigma(0))^{1/2}$ on a log-log scale for t between 0 and 0.3383. As can be seen in

https://doi.org/10.1017/S0022112001007170 Published online by Cambridge University Press

the plot, the surface average smooths out the local jumps in Mach number across shock-shocks, and the rate of increase in the average Mach number agrees well with that given by an unperturbed converging spherical shock (the dashed line with slope $-2/n$ in the figure).

The implication of the calculations in this section is that there is a tendency for converging shocks to form nearly planar pieces so that the stability result suggested by the numerical results of §4 appears to be general.

6. Conclusions

A study of converging spherical and polyhedral shocks was conducted within the theory of geometrical shock dynamics. For the polyhedral case, an analytical and numerical analysis was carried out for an equivalent problem involving an initially planar shock propagating in a converging channel with triangular cross-section. It was shown that the initial shock evolved into a repeating sequence of shock surfaces consisting of nearly planar shock pieces connected by shock-shocks, and that the increase in strength of the shocks followed the same behaviour as that for a converging spherical shock independent of the convergence angle of the channel. It was concluded that this solution is analogous to the exact solution discussed in Schwendeman & Whitham (1987) for converging shocks whose initial shape takes the form of regular polygons. The fact that the repeating surfaces in the solution for the polyhedral case involve non-planar pieces in contrast to the planar shock surfaces in the exact solution for the polygonal case is not entirely surprising and is reminiscent of the difference between the leading shock surfaces for conical and planar Mach reflection (see Hornung & Schwendeman 2001, for example). An important implication suggested by the numerical solution for the converging channel is that a spherical shock is stable to perturbations that take the form of regular polyhedra. It was noted in § 4 that this result is an extension of the stability result established in the earlier paper for the cylindrical case.

Numerical results were presented for converging spherical shocks with smooth initial perturbations in shock strength. For a case in which the perturbation possessed the same symmetry as an icosahedron, it was shown that the solution evolved into the same repeating sequence as found previously for the corresponding case of a converging channel with $\phi = 37.38^\circ$. This numerical result provides strong evidence that the repeating solution is the stable one for converging spherical shocks subject to smooth perturbations with the symmetry of regular polyhedra. A second case was considered in which the perturbation had only a reflectional symmetry so that the point of convergence was unchanged from the unperturbed solution. In this latter case, it was found that the shock developed nearly planar surfaces, and an average shock strength was calculated and shown to increase at a rate nearly equal to that of an unperturbed converging spherical shock. The conclusion supported by both cases is that converging spherical shocks are stable to smooth initial perturbations in shock strength.

Finally, it is noted that the numerical method developed here to compute converging shocks has a wider range of applicability. The method enjoys the flexibility of an unstructured grid and may be used to compute three-dimensional shock propagation for a wide variety of geometric configurations. In addition, the method could be extended, following the work in Schwendeman (1999) for example, to handle shock propagation in gases with non-uniform properties ahead of the shock.

https://doi.org/10.1017/S0022112001007170 Published online by Cambridge University Press

REFERENCES

Apazidis, N. & Lesser, M. B. 1996 On generation and convergence of polygonal-shaped shock waves. *J. Fluid Mech.* **309**, 301–319.

Chester, W. 1954 The quasi-cylindrical shock tube. *Phil. Mag.* **45**, 1293–1301.

Chisnell, R. F. 1957 The motion of a shock wave in a channel, with applications to cylindrical and spherical shocks. *J. Fluid Mech.* **2**, 286–298.

Fong, K. & Ahlborn, B. 1979 Stability of converging shock waves. *Phys. Fluids* **22**, 416–421.

Gardner, J. H., Book, D. L. & Bernstein, I. B. 1982 Stability of imploding shocks in the CCW approximation. *J. Fluid Mech.* **114**, 41–58.

Godunov, S. K. 1959 Difference methods for the numerical calculation of the equations of fluid dynamics. *Mat. Sb.* **47**, 271–306.

Guderley, G. 1942 Starke kugelige und zylindrische Verdichtungsstösse in der Nähe des Kugelmittelpunktes bzw der Zylinderachse. *Luftfahrtforschung* **19**, 302–312.

Hornung, H. G. & Schwendeman, D. W. 2001 Oblique shock reflection from an axis of symmetry: shock dynamics and relation to the Guderley singularity. *J. Fluid Mech.* **438**, 231–245.

Schwendeman, D. W. 1988 A numerical scheme for shock propagation in three dimensions. *Proc. R. Soc. Lond.* A **416**, 179–198.

Schwendeman, D. W. 1993 A new numerical method for shock wave propagation based on geometrical shock dynamics. *Proc. R. Soc. Lond.* A **441**, 331–341.

Schwendeman, D. W. 1999 A higher-order Godunov method for the hyperbolic equations modelling shock dynamics. *Proc. R. Soc. Lond.* A **455**, 1215–1233.

Schwendeman, D. W. & Whitham, G. B. 1987 On converging shock waves. *Proc. R. Soc. Lond.* A **413**, 297–311.

Takayama K., Kleine, H. & Grönig, H. 1987 An experimental investigation of the stability of converging cylindrical shock waves in air. *Exps. Fluids* **5**, 315–322.

Watanabe, M. & Takayama, K. 1991 Stability of converging cylindrical shock waves. *Shock Waves* **1**, 149–160.

Whitham, G. B. 1957 A new approach to problems of shock dynamics. Part 1. Two-dimensional problems. *J. Fluid Mech.* **2**, 145–171.

Whitham, G. B. 1974 *Linear and Nonlinear Waves*. John Wiley & Sons.

https://doi.org/10.1017/S0022112001007170 Published online by Cambridge University Press